PHOTONICS Research

Narrowband photonic quantum entanglement with counterpropagating domain engineering

YI-CHEN LIU,[1,†] DONG-JIE GUO,[1,†] RAN YANG,[1] CHANG-WEI SUN,[1] JIA-CHEN DUAN,[1] YAN-XIAO GONG,[1,2] ZHENDA XIE,[1,3] AND SHI-NING ZHU[1]

[1]National Laboratory of Solid State Microstructures, School of Electronic Science and Engineering, School of Physics, Collaborative Innovation Center of Advanced Microstructures, Nanjing University, Nanjing 210093, China
[2]e-mail: gongyanxiao@nju.edu.cn
[3]e-mail: xiezhenda@nju.edu.cn

Received 20 October 2020; revised 27 June 2021; accepted 23 July 2021; posted 23 July 2021 (Doc. ID 413075); published 16 September 2021

Narrowband photonic entanglement is a crucial resource for long-distance quantum communication and quantum information processing, including quantum memories. We demonstrate the first polarization entanglement with 7.1 GHz inherent bandwidth by counterpropagating domain engineering, which is also confirmed by Hong–Ou–Mandel interference with 155-ps base-to-base dip width and (97.1 ± 0.59)% high visibility. The entanglement is harnessed with 18.5-standard-deviations Bell inequality violation, and further characterized with state tomography of (95.71 ± 0.61)% fidelity. Such narrowband entanglement sets a cornerstone for practical quantum information applications.

https://doi.org/10.1364/PRJ.413075

1. INTRODUCTION

Quantum entanglement is the basis of fundamental quantum mechanics studies and quantum information technologies [1–3]. So far, the most developed entangled sources are via the optical approach because of its low decoherence and high purity. However, the entangled photon source needs to be compatible with information-processing devices for practical applications, where the photon–electron interaction is normally required. One important example is the memory [4–6] for quantum information, which is not only essential for quantum computation [7,8], but also necessary to realize quantum repeaters for long-distance quantum communication [9–12]. It is the ultimate solution to overcome the inevitable photon loss over large communication distances and regain the channel security and data rate. In the above cases, the bandwidth of such photon–electron interaction is fundamentally limited by the energy level of the electrons. The recent breakthrough in the solid-state quantum memories has pushed this bandwidth limit to the order of gigahertz [13–18], though such bandwidth is still too narrow for the conventional entangled photon sources based on spontaneous parametric downconversion (SPDC) [19,20]. Much effort has been devoted to shrinking the biphoton bandwidth, such as passive filtering [21,22] or cavity enhancement [23]. But it either reduces the brightness, or adds complexity and instability of the system. On the other hand, the counterpropagating phase-matching [24] geometry can inherently reduce the phase-matching bandwidth [25–28] without cavity interactions. This geometry relies on the optical microstructure manufacture, and such counterpropagating domain engineering has been demonstrated for mirrorless optical parametric oscillation [29] and SPDC [30–33].

Here we report the first narrowband photonic polarization entanglement generation using counterpropagating domain engineering. The state-of-the-art manufacture of 1.3 μm poling period in a Type II periodically poled potassium titanyl phosphate (PPKTP) waveguide enables 7.1 GHz biphoton bandwidth at telecom wavelength, as well as the deterministic separation of the counterpropagating signal and idler photons even at wavelength degeneracy. The bandwidth is directly measured in the spectral domain with scanning narrow-line filters, and also confirmed with the Hong–Ou–Mandel (HOM) interference [34]. Its high visibility of $(97.1 \pm 0.59)\%$ reveals the generation of high-quality identical photon pairs. With a bidirectional pump, polarization entanglement can be constructed, with the Clauser–Horne–Shimony–Holt S-parameter of 2.720 ± 0.039. The state tomography further shows a high state fidelity of $(95.71 \pm 0.61)\%$. This entangled state fulfills the bandwidth requirement of solid-state quantum memories and is thus important for the quantum information processing and communication.

2. EXPERIMENTAL SETUP

In experiment, the PPKTP waveguide is designed for Type II quasi-phase matching (QPM) backward spontaneous parametric downconversion (BSPDC). The waveguide was fabricated by ion implantation in ADVR Inc., with a length of 10 mm.

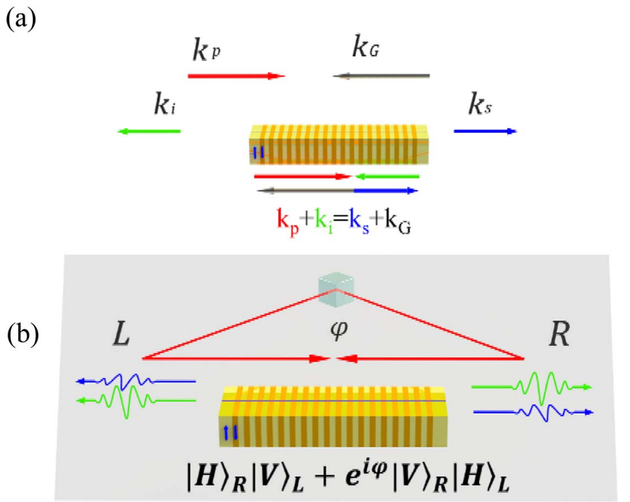

Fig. 1. Scheme of the counterpropagating polarization-entangled photon source. (a) Phase-matching diagram of the BSPDC; (b) polarization entanglement generation from the BSPDC with bidirectional pump light.

To avoid spurious back reflections from the waveguide end faces, the sample is angle-polished at 10°. The poling length is also 10 mm, and the period is designed to be 1.3 μm. The measured coupling efficiency into/out of the waveguide is about 20% and 50% for laser light at 780 and 1550 nm, respectively. As illustrated in Fig. 1(a), a forward pump photon can generate a forward signal photon and a backward idler photon with polarizations along the y, y, and z axes of the potassium titanyl phosphate (KTP) crystal, respectively. The corresponding phase matching requires a large reciprocal vector, thus, an ultrashort poling period. For our design, this BSPDC process can be phase-matched with the third-order reciprocal vector of the 1.3 μm poling period in the PPKTP waveguide. The QPM condition for BSPDC is

$$\Delta k = k_{p0} - k_{s0} + k_{i0} - \frac{6\pi}{\Lambda} = 0, \tag{1}$$

where k_{j0}, $j = p, s, i$, are the pump, signal, and idler wave vectors at the center frequencies, respectively. As shown in Fig. 1(b), the horizontal (H) and vertical (V) polarizations correspond to the KTP y and z axes, respectively. With the bidirectional pump at frequency degeneracy, two Type II BSPDC processes can happen with reversed directions, thus resulting in

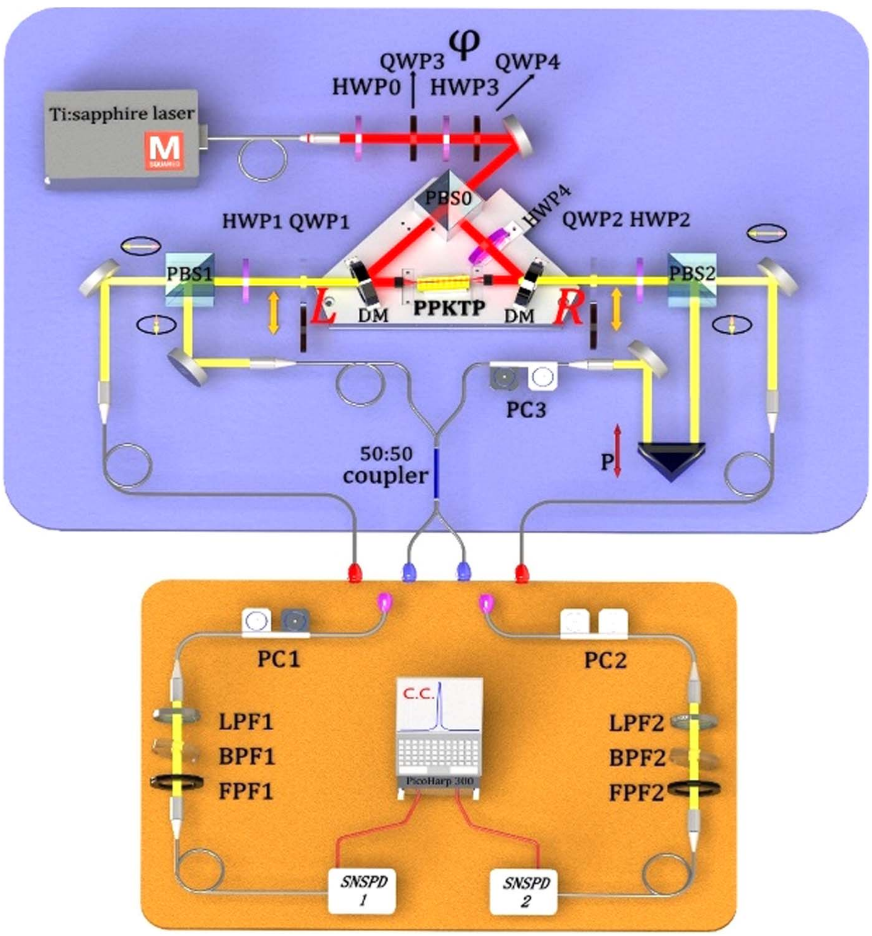

Fig. 2. Experimental setup. HWP, half-wave plate; QWP, quarter-wave plate; PBS, polarization beam splitter; DM, dichroic mirror; PC, polarization controller; LPF, long-pass filter; BPF, bandpass filter; FPF, Fabry–Perot filter; P, prism; SNSPD, superconducting nanowire single-photon detector; C.C., coincidence counts.

the generation of the polarization-entangled state $|\Psi\rangle = (|H\rangle_R|V\rangle_L + e^{i\varphi}|V\rangle_R|H\rangle_L)/\sqrt{2}$, where the subscripts R and L denote the right and left propagating directions, respectively. Here the phase φ is determined by the relative phase difference between the bidirectional pump beams.

Our experiment setup is shown in Fig. 2. The pump light is from a continuous-wave Ti:sapphire laser (SolsTis) and transmits in a triangle loop with the polarization beam splitter (PBS0). The power ratio between the R and L is controlled by rotating the optical axis angle of a half-wave plate (HWP0), and the relative phase can be finely tuned by the optical axis angle of HWP3 sandwiched between two 45° quarter-wave plates (QWP3 and QWP4). HWP4 is oriented as 45° to rotate pump polarization to H for SPDC. Then the two pump light beams are reflected by two dichroic mirrors (DMs) and coupled into the PPKTP waveguide in two opposite directions. The above state preparation setup is integrated on a solid metal housing, where the temperature is finely controlled by Peltier elements within accuracy of milli-Kelvin level. Therefore, the phase difference in the pump loop can be stabilized. The DMs are designed for high transmission for BSPDC outputs at telecom wavelengths, for direct output at R and L ports. The output photon pairs are then detected by two superconducting nanowire single-photon detectors (SNSPDs) with efficiencies over 90% at 1550 nm. Filter sets are used in the R and L ports for spectral cleaning, including a long-pass filter (Thorlabs FEL0900), a bandpass filter (Semrock NIR01-1570/3-25), and a homemade Fabry–Perot filter (FPF) (for details, see Appendix A) in each set.

3. RESULTS

We first check the phase matching of the PPKTP waveguide by the backward second-harmonic generation (SHG) process. A tunable semiconductor laser (Santec TSL-710) with a linewidth of 100 kHz is used as the fundamental light (FL). It is first split into two beams and coupled into the waveguide through the R and L BSPDC output ports, which are set to V and H polarizations, respectively, so that the SHG light is phase-matched for the right propagation. By varying the laser wavelength, we record the SHG output power with a power meter (Thorlabs S154C) as a function of fundamental wavelength. As shown in Fig. 3, when the fundamental wavelength was tuned to 1553.48 nm, a maximum SHG output power of 99.5 nW was obtained. The main peak agrees well with the theoretical simulation from the function $\text{sinc}^2(\Delta k_{\text{SHG}}L/2)$, where $\Delta k_{\text{SHG}} = k_{\text{SHG},H} + k_{\text{FL},H} - k_{\text{FL},V} - 6\pi/\Lambda$ is the phase mismatch in the SHG process. The nonideal satellite peaks could result from fabrication imperfections. The normalized SHG conversion efficiency can be calculated according to $\eta_{\text{SHG}} = P_{\text{SHG}}/(P_{\text{FL},H}\,P_{\text{FL},V})$, where the FL powers are $P_{\text{FL},H} = 13\,\text{mW}$ and $P_{\text{FL},V} = 13.5\,\text{mW}$ at the maximum SHG power of $P_{\text{SHG}} = 99.5\,\text{nW}$. Thus, the peak efficiency of SHG is about $\eta_{\text{SHG,max}} = 5.67\times10^{-4}\,\text{W}^{-1}$. With pump wavelength fixed at 776.74 nm, we expect to obtain the required frequency-degenerate BSPDC that is a reversed nonlinear optical process of SHG, namely, $H_{776.74\,\text{nm}} \rightarrow H_{1553.48\,\text{nm}} + V_{1553.48\,\text{nm}}$.

For simplicity, we focus on the BSPDC pumped in a single direction by setting HWP0 to 0°. The BSPDC spectrum

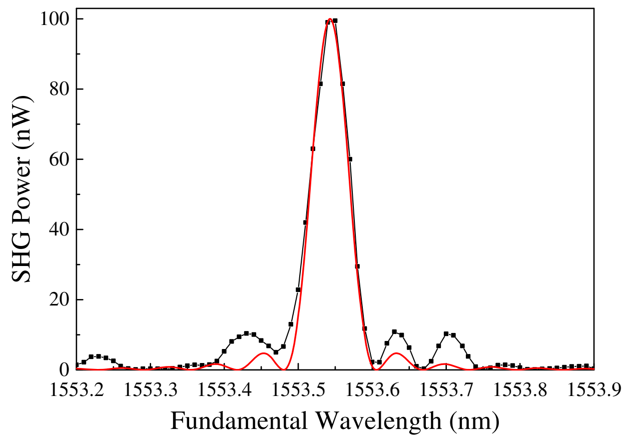

Fig. 3. SHG measurement. SHG output power as a function of FL wavelength. The red curve is a sinc^2-function fit.

characterization is performed by scanning a homemade Fabry–Perot cavity (FPC) with a FWHM linewidth of 7.8 pm (for details, see Appendix A). This FPC transmission is much narrower than the bandwidth of BSPDC, where the transmitted signal or idler frequency can be tuned by varying its temperature. The BSPDC spectrum is achieved in a coincidence measurement for the best signal-to-noise ratio during the FPC scan. The measured signal and idler photon spectra are shown in Fig. 4(a), with identical bandwidth fitted to be 57 pm (7.1 GHz). Their central wavelengths can be finely tuned to match each other by varying the PPKTP waveguide temperature. The satellite peaks are higher than the expectations and nonsymmetric, which is due to fabrication imperfections of the waveguide. To clean the nonideal satellite peaks, we insert a pair of 100 μm thick FPFs (for details, see Appendix A). As shown in the Fig. 4(a) inset, the FWHM linewidth of each FPF is measured to be about 132 pm, which is larger than the 57 pm BSPDC bandwidth, and thus does not affect the central spectrum of the source.

The quantum feature of a two-photon source can be presented by a high-visibility quantum interference. Here it is tested using the HOM interferometer, and the narrow bandwidth of the BSPDC spectrum can be also characterized from the correlation time in the interference measurement. Keeping the single-direction-pumped setup, we set the polarizations of the L and R output ports to make photons be reflected at PBS1 and PBS2, so that the BSPDC light is directed to a 50:50 fiber coupler for the HOM interference. A fiber polarization controller (PC3) is used to make the polarization of the two arms identical. The relative delay Δt is controlled by a motorized optical delay line in the idler photon arm. The outputs of the HOM interferometer are coupled to SNSPD for coincidence measurement. The coincidence counts in 15 s as a function of Δt are presented in Fig. 4(b), and the visibility is calculated to be $(90.1 \pm 0.91)\%$, or $(97.1 \pm 0.59)\%$ after subtracting the accidentals. A triangle fit of the HOM dip shows a base-to-base dip width of 155 ps. This result agrees well with the 7.1 GHz BSPDC bandwidth in the spectrum measurement.

The spectrum and HOM interference measurements directly show that we do produce photon pairs with narrow

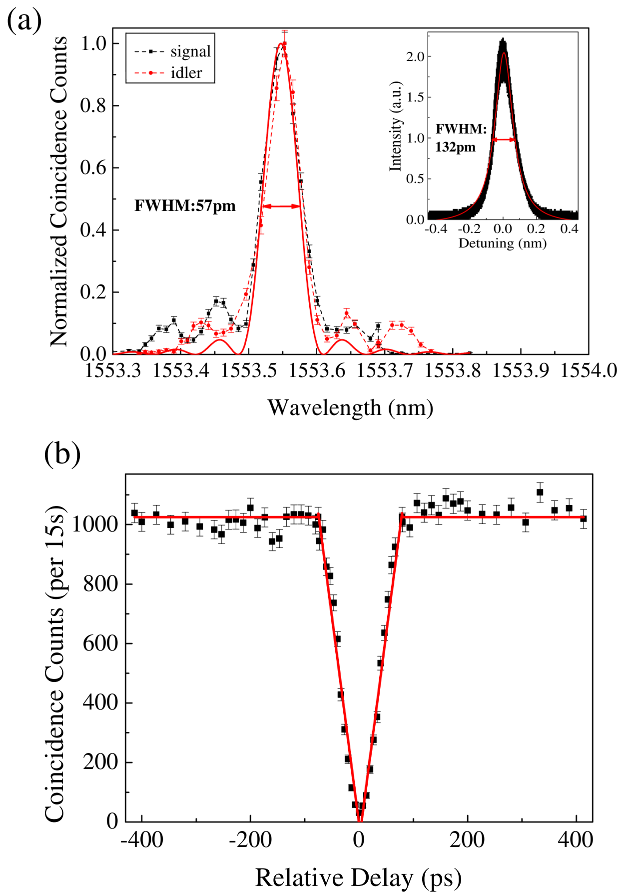

Fig. 4. BSPDC measurements. (a) Measurement of BSPDC spectrum. Black and red dots correspond to signal and idler photon spectra, respectively. The curve is fitted to sinc^2 functions in solid curves. Inset, transmission spectrum of the FPF for spectral cleaning. (b) Quantum interference measurement with HOM interferometer. The HOM dip is fitted to a triangle function.

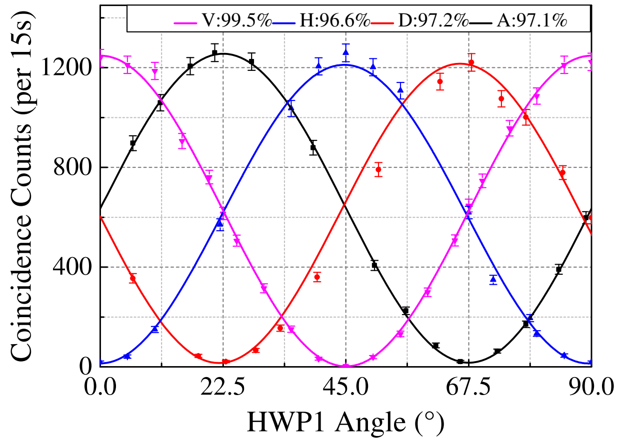

Fig. 5. Entanglement correlation measurement. Coincidence counts are recorded as a function of HWP1 angle for changing the linear polarization projection measurement on one photon with the other photon projected to four states: H (blue), V (pink), D (red), and A (black), respectively. The curves are fitted with sine and cosine functions.

bandwidth in the BSPDC process. Then we can produce the polarization entanglement by rotating HWP0 away from 0°, and here we fix it at 45° for maximum entanglement generation, and adjust HWP3 to generate the singlet state $|\Psi^-\rangle = (|H\rangle_\mathrm{R}|V\rangle_\mathrm{L} - |V\rangle_\mathrm{R}|H\rangle_\mathrm{L})/\sqrt{2}$.

We first characterize the entanglement via polarization correlation measurement, where HWP2 is set to 0°, 45°, and ±22.5° to project the R photon to H, V, and ±45° polarization states, respectively. Under each projection, we record the coincidence counts against the angle of HWP1 for projection measurement on the L photon. The measured interference fringes are shown in Fig. 5, which all fit well with sine and cosine functions, with visibilities calculated to be $(96.6 \pm 0.45)\%$, $(99.5 \pm 0.19)\%$, $(97.2 \pm 0.53)\%$, and $(97.1 \pm 0.53)\%$, respectively. With 10 mW pump, the maximum coincidence rate exceeds 1260 counts in 15 s, and the total photon collection efficiency is about 2%, corresponding to a source brightness of 3.4 kHz/(GHz · mW). Then we perform the Clauser–Horne–Shimony–Holt (CHSH)-type Bell inequality test [35], and obtain an S value of 2.720 ± 0.039, indicating a violation of the Bell inequality by 18.5 standard deviations.

We further characterize the entanglement state using the standard quantum state tomography [36]. By inserting QWP1 and QWP2 in the L and R outputs, we can perform projection measurements on the four states $|H\rangle$, $|V\rangle$, $|D\rangle = (|H\rangle + |V\rangle)/\sqrt{2}$, and $|R\rangle = (|H\rangle - i|V\rangle)/\sqrt{2}$ for each photon separately, and record the coincidence counts for all the combinations. The reconstructed real and imaginary parts of the density matrix ρ_e are shown in Fig. 6, with the fidelity [37] calculated as $F(\rho_e, |\Psi^-\rangle) = \langle\Psi^-|\rho_e|\Psi^-\rangle = (95.71 \pm 0.61)\%$. Note that the above errors are estimated by considering a Poisson fluctuation in our data measurement. The above polarization measurements confirm high-fidelity polarization entanglement generation, which is achieved in narrow bandwidth without cavities for the first time.

Our photonic polarization-entangled source relies on the superposition of two bidirectional BSPDC processes. As shown in Fig. 1(b), the superposition phase stability depends on the optical length difference between two pump arms from PBS0 to the PPKTP waveguide, which needs to be stabilized to subwavelength level. It is achieved by the balanced design in the two arms, and the whole source sits on a monolithic aluminum housing for temperature equilibrium. This design greatly

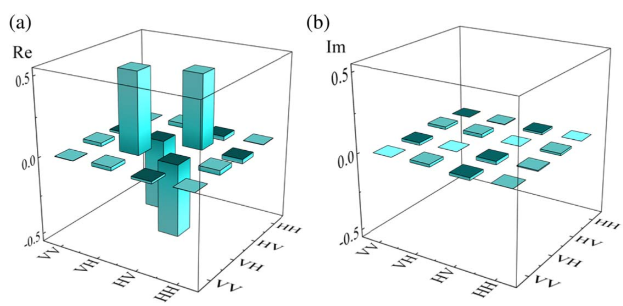

Fig. 6. (a) Real and (b) imaginary parts of the reconstructed density matrix for the produced polarization entanglement state.

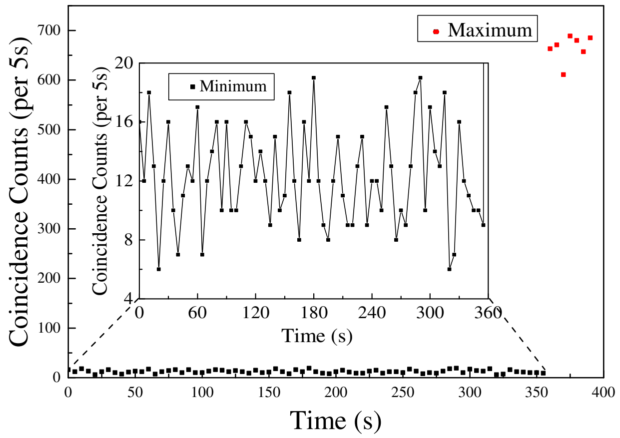

Fig. 7. Phase stability test. Coincidence counts for $|DD\rangle$ (black square dots) and $|DA\rangle$ (red dots) projection measurements. The inset is a zoom-in for $|DD\rangle$ measurement in 6 min.

cancels the phase sensitivity of the temperature change. For further stabilization, our source is built with the temperature stabilized by a Peltier cooler and sealed in a metal box. By using high-performance temperature controllers, the entangled source can be stabilized to milli-Kelvin level.

To test the phase stability, we project the entangled photons on the $\pm 45°$ polarization basis states $|D/A\rangle = (|H\rangle \pm |V\rangle)/\sqrt{2}$, and measure the twofold coincidence. For the target singlet state $|\Psi^-\rangle = (|H\rangle_R|V\rangle_L - |V\rangle_R|H\rangle_L)/\sqrt{2}$, minimum and maximum coincidence counts are obtained in the $|DD\rangle$ and $|DA\rangle$ measurements, respectively. As shown in Fig. 7, the visibility stays higher than 97% in 6 min, corresponding to a phase fluctuation of less than 1°. The test verifies the high phase-stability of our source.

4. CONCLUSION AND DISCUSSION

We have demonstrated the first narrowband photonic quantum entanglement generation by the state-of-the-art backward domain engineering in a PPKTP waveguide. The BSPDC geometry enables an inherent bandwidth of 7.1 GHz as well as deterministic separation of collinear frequency-degenerate polarization-entangled photon pairs. A phase-stabilized bidirectional pump can be easily achieved in balanced arm loop with only temperature control. We show an example of singlet state generation with a fidelity of $(95.71 \pm 0.61)\%$, which can be generalized to any arbitrary polarization-entangled photon pair state in our setup. In this work, our fabrication is limited by the current lithography capability to the third-order QPM for the BSPDC realization, where the spectral brightness of the photonic entanglement exceeds 3.4 kHz/(GHz·mW). Further improvement on the source brightness is possible with better fabrication toward first-order QPM, which can increase the brightness by 9 times. In Table 1, we list several narrowband polarization-entangled photon sources [38–44]. We can see that our source shows the advantage of preparing narrowband photons compared to the conventional PDC approaches. Our result is already comparable with cavity-enhanced experiments in conventional QPM geometry [43,44], while the cavity-enhanced sources are greatly complex with the cavity locking optics and electronics, and requires the postselection technique to produce polarization entanglement.

The counterpropagating domain engineering can also be adopted into the fast-developing lithium liobate thin-film platform, and the tight mode confinement can further boost the conversion efficiency in a much smaller footprint for large-scale integration. Therefore, it is a unique and powerful tool for narrowband photonic quantum entanglement generation, which links the photonic qubits to other key elements in the quantum information processing that requires photon–electron interaction, including quantum memory, which is important for quantum information technologies.

APPENDIX A: FABRY–PEROT RESONATORS FOR BSPDC SPECTRUM MEASUREMENT AND CLEANING

We develop two types of Fabry–Perot resonators for the BSPDC spectrum measurement and cleaning, which are called the FPC and the FPF, respectively. Both resonators are double-sided coated plate (etalon) made of lithium niobate and polished to the thickness as required. The FPC has a linewidth much smaller than the BSPDC bandwidth, so that it can scan across the BSPDC spectrum, while the FPF linewidth is designed larger than the BSPDC bandwidth so that BSPDC spectral feature does not change after cleaning. The free spectral range (FSR) of the FPF is designed larger than the bandpass filter linewidth for best noise reduction.

High finesse is required for both resonators to achieve a high rejection ratio. From the coating design, the FPC and FPF have target finesses of 155.5 and 50.8, respectively. High-quality mechanical polishing and coating techniques are required to

Table 1. List of Narrowband Polarization-Entangled Photon Sources

Polarization-Entangled Photon Source	Method	Wavelength (nm)	Bandwidth	Brightness [Hz/(mW · MHz)]	Fidelity
Fedrizzi *et.al.* [38]	Sagnac interferometer	810	137 GHz	0.597	99.78%
Kuzucu *et al.* [39]	Sagnac interferometer	780.7	73.8 GHz	4.22	98.85%
Sansoni *et al.* [40]	Two periodically poled waveguides	1554	260 GHz	38.7	97.3%
Herrmann *et al.* [41]	Biperiodic poling waveguide	1551/1571	85 GHz	7	97.5%
Sun *et al.* [42]	Dual-periodic poling waveguide	1489.9/1335	270 GHz	42	94.5%
Bao *et al.* [43]	Cavity and postselection	780	9.6 MHz	6	94%
Tian *et al.* [44]	Cavity and postselection	795	15 MHz	3	95.2%
This work	Counter propagating	1553.5	7.1 GHz	3.4	95.7%

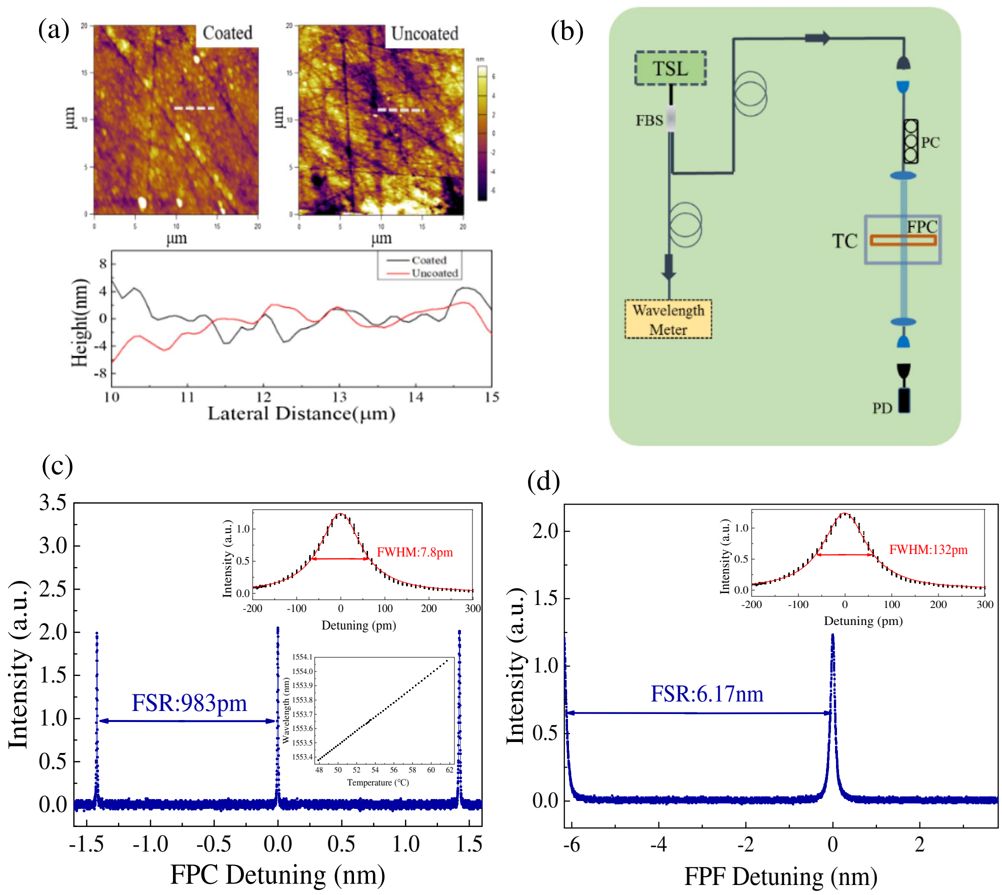

Fig. 8. Characterization of the two Fabry–Perot resonators. (a) AFM image of FPC before and after coating; (b) Fabry–Perot resonator test setup. TSL, tunable semiconductor laser; PC, polarization controller; TC, temperature controller; FPC, Fabry–Perot cavity; FBS, fiber beam splitter; PD, photodetector. (c) FPC transmission intensity as a function of wavelength detuning from the center transmission peak. The upper inset shows the zoom-in of one transmission peak of 7.8 pm linewidth, and the lower inset is the measured temperature-wavelength relationship. (d) Transmission measurements for the FPF, with 6.17 nm FSR and 132 pm linewidth for the transmission peak.

Table 2. Characterization of the FPC and FPF.

Sample	Cavity Length (μm)	Reflectivity	Theoretical Linewidth (GHz)	Theoretical Finesse	Experimental Finesse	Cutoff (dB)
FPC	400	98%	1.1	155.5	125.6	30
FPF	100	94%	13.1	50.8	46.7	30

achieve that. As shown in Fig. 8(a), we use atomic force microscopy (AFM) to measure the surface roughness before and after coating, with results of 2.95 and 2.81 nm, respectively, in root mean square (RMS) values within the 5 μm area. In experiment, the FPC and FPF attain a finesse of 125.6 and 46.7, respectively, showing the high-quality fabrication for both devices, as shown in Table 2. Both resonators are cut to a suitable size and are finally mounted in thermal conductive metal housings with thermoelectric coolers for precise temperature control. Since the refractive index changes with the temperature, we can change the transmission wavelength of the FPC, which is used as a tunable filter in our experiment.

We use a wavelength-tunable cw laser (Santec TSL-710) with a narrow linewidth of 100 kHz to scan the resonances, with absolute wavelength calibration using a wavelength meter (HighFinesse WS-6), as shown in Fig. 8(b). Both resonators are connected to the fiber via the fiber–space–fiber coupling method with two lenses, and the peak transmittance is about 50%. The scan results of the FPC are shown in Fig. 8(c), and the FSR is measured to be 0.983 nm (122 GHz), which agrees well with the 400 μm cavity length. The inset shows the zoom-in of a resonance, and the FPC linewidth is fitted to be 7.8 pm (0.96 GHz), which is about one-tenth of the BSPDC bandwidth. Such fineness is sufficient to scan the BSPDC spectrum.

The relationship between the FPC temperature and its transmission peak is shown in the bottom inset of Fig. 8(c). By adjusting the temperature from 48°C to 62°C, the transmission peak can be tuned from 1553.4 to 1554.1 nm. We perform similar measurements for the FPF. The results are shown in Fig. 8(d), with FSR and linewidth measured to be 6.17 nm (767 GHz) and 132 pm (16.5 GHz), respectively, which agree with the theoretical expectation. With such a large FSR, the FPF can pair with the bandpass filter for a broadband background photon suppression.

Funding. National Key Research and Development Program of China (2017YFA0303700); Key R&D Program of Guangdong Province (2018B030329001); National Natural Science Foundation of China (11474050, 11674169, 11974178, 51890861).

Acknowledgment. ZDX, YXG, and YCL conceived and designed the experiment. YCL, DJG, RY, CWS, and JCD performed the experimental measurements. SNZ, ZDX, and YXG supervised the project. YCL and DJG wrote the paper, with contributions from all authors.

Disclosures. The authors declare no competing interest.

†These authors contributed equally to this work.

REFERENCES

1. J. L. O'Brien, A. Furusawa, and J. Vuckovic, "Photonic quantum technologies," Nat. Photonics **3**, 687–695 (2009).
2. J. I. Cirac, A. K. Ekert, S. F. Huelga, and C. Macchiavello, "Distributed quantum computation over noisy channels," Phys. Rev. A **59**, 4249–4254 (1999).
3. N. Gisin, G. G. Ribordy, W. Tittel, and H. Zbinden, "Quantum cryptography," Rev. Mod. Phys. **74**, 145–195 (2002).
4. A. I. Lvovsky, B. C. Sanders, and W. Tittel, "Optical quantum memory," Nat. Photonics **3**, 706–714 (2009).
5. X.-M. Jin, J.-G. Ren, B. Yang, Z.-H. Yi, F. Zhou, X.-F. Xu, S.-K. Wang, D. Yang, Y.-F. Hu, S. Jiang, T. Yang, H. Yin, K. Chen, C.-Z. Peng, and J.-W. Pan, "Experimental free-space quantum teleportation," Nat. Photonics **4**, 376–381 (2010).
6. N. Gisin and R. Thew, "Quantum communication," Nat. Photonics **1**, 165–171 (2007).
7. E. Knill, R. Laflamme, and G. J. Milburn, "A scheme for efficient quantum computation with linear optics," Nature **409**, 46–52 (2001).
8. P. Kok, W. J. Munro, K. Nemoto, T. C. Ralph, J. P. Dowling, and G. J. Milburn, "Linear optical quantum computing with photonic qubits," Rev. Mod. Phys. **79**, 135–174 (2007).
9. L.-M. Duan, M. D. Lukin, J. I. Cirac, and P. Zoller, "Long-distance quantum communication with atomic ensembles and linear optics," Nature **414**, 413–418 (2001).
10. H. J. Briegel, W. Dur, J. I. Cirac, and P. Zoller, "Quantum repeaters: the role of imperfect local operations in quantum communication," Phys. Rev. Lett. **81**, 5932–5935 (1998).
11. C. Jones, D. Kim, M. T. Rakher, P. G. Kwiat, and T. D. Ladd, "Design and analysis of communication protocols for quantum repeater networks," New J. Phys. **18**, 083015 (2016).
12. H. J. Kimble, "The quantum internet," Nature **453**, 1023–1030 (2008).
13. E. Saglamyurek, J. Jin, V. B. Verma, M. D. Shaw, F. Marsili, S. W. Nam, D. Oblak, and W. Tittel, "Quantum storage of entangled telecom-wavelength photons in an erbium-doped optical fibre," Nat. Photonics **9**, 83–87 (2015).
14. J. Jin, E. Saglamyurek, M. L. Puigibert, V. Verma, F. Marsili, S. W. Nam, D. Oblak, and W. Tittel, "Telecom-wavelength atomic quantum memory in optical fiber for heralded polarization qubits," Phys. Rev. Lett. **115**, 140501 (2015).
15. E. Saglamyurek, N. Sinclair, J. Jin, J. A. Slater, D. Oblak, F. Bussieres, M. George, R. Ricken, W. Sohler, and W. Tittel, "Broadband waveguide quantum memory for entangled photons," Nature **469**, 512–515 (2011).
16. M. F. Askarani, M. L. G. Puigibert, T. Lutz, V. B. Verma, M. D. Shaw, S. W. Nam, N. Sinclair, D. Oblak, and W. Tittel, "Storage and reemission of heralded telecommunication-wavelength photons using a crystal waveguide," Phys. Rev. Appl. **11**, 054056 (2019).
17. M. Rančić, M. P. Hedges, R. L. Ahlefeldt, and M. J. Sellars, "Coherence time of over a second in a telecom-compatible quantum memory storage material," Nat. Phys. **14**, 50–54 (2017).
18. M. P. Hedges, J. J. Longdell, Y. Li, and M. J. Sellars, "Efficient quantum memory for light," Nature **465**, 1052–1056 (2010).
19. C. Kurtsiefer, M. Oberparleiter, and H. Weinfurter, "High-efficiency entangled photon pair collection in type-II parametric fluorescence," Phys. Rev. A **64**, 023802 (2001).
20. S. Tanzilli, H. D. Riedmatten, W. Tittel, H. Zbinden, P. Baldi, M. D. Micheli, D. B. Ostrowsky, and N. Gisin, "Highly efficient photon-pair source using periodically poled lithium niobate waveguide," Electron. Lett. **37**, 26–28 (2001).
21. M. Halder, A. Beveratos, N. Gisin, V. Scarani, C. Simon, and H. Zbinden, "Entangling independent photons by time measurement,". Nat. Phys. **3**, 692–695 (2007).
22. M. Halder, S. Tanzilli, H. D. Riedmatten, A. Beveratos, H. Zbinden, and N. Gisin, "Photon-bunching measurement after two 25-km-long optical fibers," Phys. Rev. A **71**, 042335 (2005).
23. M. Scholz, L. Koch, and O. Benson, "Statistics of narrow-band single photons for quantum memories generated by ultrabright cavity-enhanced parametric down-conversion," Phys. Rev. Lett. **102**, 063603 (2009).
24. S. E. Harris, "Proposed backward wave oscillation in the infrared," Appl. Phys. Lett. **9**, 114–116 (1966).
25. A. Christ, A. Eckstein, P. J. Mosley, and C. Silberhorn, "Pure single photon generation by type-I PDC with backward-wave amplification," Opt. Express **17**, 3441–3446 (2009).
26. Y.-X. Gong, Z.-D. Xie, P. Xu, X.-Q. Yu, P. Xue, and S.-N. Zhu, "Compact source of narrow-band counter propagating polarization-entangled photon pairs using a single dual-periodically-poled crystal," Phys. Rev. A **84**, 053825 (2011).
27. M. C. Booth, M. Atature, G. D. Giuseppe, B. E. A. Saleh, A. V. Sergienko, and M. C. Teich, "Counterpropagating entangled photons from a waveguide with periodic nonlinearity," Phys. Rev. A **66**, 023815 (2002).
28. W.-H. Cai, B. Wei, S. Wang, and R.-B. Jin, "Counter-propagating spectrally uncorrelated biphotons at 1550 nm generated from periodically poled $MTiOXO_4$ (M = K, Rb, Cs; X = P, As)," J. Opt. Soc. Am. B **37**, 3048–3054 (2020).
29. C. Canalias and V. Pasiskevicius, "Mirrorless optical parametric oscillator," Nat. Photonics **1**, 459–462 (2007).
30. L. Lanco, S. Ducci, J. P. Likforman, X. Marcadet, J. A. Houwelingen, H. Zbinden, G. Leo, and V. Berger, "Semiconductor waveguide source of counterpropagating twin photons," Phys. Rev. Lett. **97**, 173901 (2006).
31. A. A. Shukhin, I. Z. Latypov, A. V. Shkalikov, and A. A. Kalachev, "Simulating single-photon sources based on backward-wave spontaneous parametric down-conversion in a periodically poled KTP waveguide," Epj. Web. Conf. **103**, 012015 (2015).
32. K. H. Luo, V. Ansari, M. Massaro, M. Santandrea, C. Eigner, R. Ricken, H. Herrmann, and C. Silberhorn, "Counter-propagating photon pair generation in a nonlinear waveguide," Opt. Express **28**, 3215–3225 (2020).
33. S. Francesconi, F. Baboux, A. Raymond, N. Fabre, G. Boucher, A. Lemaître, P. Milman, M. I. Amanti, and S. Ducci, "Engineering two-photon wavefunction and exchange statistics in a semiconductor chip," Optica **7**, 316–322 (2020).
34. A. Gilchrist, N. K. Langford, and M. A. Nielsen, "Distance measures to compare real and ideal quantum processes," Phys. Rev. A **71**, 062310 (2005).

35. J. F. Clauser, M. A. Horne, A. Shimony, and R. A. Holt, "Proposed experiment to test local hidden-variable theories," Phys. Rev. Lett. **23**, 880–884 (1969).
36. D. F. V. James, P. G. Kwiat, W. J. Munro, and A. G. White, "Measurement of qubits," Phys. Rev. A **64**, 052312 (2001).
37. C. K. Hong, Z. Y. Ou, and L. Mandel, "Measurement of subpicosecond time intervals between two photons by interference," Phys. Rev. Lett. **59**, 2044–2046 (1987).
38. A. Fedrizzi, T. Herbst, A. Poppe, T. Jennewein, and A. Zeilinger, "A wavelength-tunable fiber-coupled source of narrowband entangled photons," Opt. Express **15**, 15377–15386 (2007).
39. O. Kuzucu and F. N. C. Wong, "Pulsed Sagnac source of narrow-band polarization-entangled photons," Phys. Rev. A **77**, 032314 (2008).
40. L. Sansoni, K. H. Luo, C. Eigner, R. Ricken, V. Quiring, H. Herrmann, and C. Silberhorn, "A two-channel, spectrally degenerate polarization entangled source on chip," npj Quantum Inf. **3**, 5 (2017).
41. H. Herrmann, X. Yang, A. Thomas, A. Poppe, W. Sohler, and C. Silberhorn, "Post-selection free, integrated optical source of non-degenerate, polarization entangled photon pairs," Opt. Express **21**, 27981–27991 (2013).
42. C.-W. Sun, S.-H. Wu, J.-C. Duan, J.-W. Zhou, J.-L. Xia, P. Xu, Z. Xie, Y.-X. Gong, and S.-N. Zhu, "Compact polarization-entangled photon-pair source based on a dual-periodically-poled Ti:$LiNbO_3$ waveguide," Opt. Lett. **44**, 5598–5601 (2019).
43. X.-H. Bao, Y. Qian, J. Yang, H. Zhang, Z.-B. Chen, T. Yang, and J.-W. Pan, "Generation of narrow-band polarization-entangled photon pairs for atomic quantum memories," Phys. Rev. Lett. **101**, 190501 (2008).
44. L. Tian, S. Li, H. Yuan, and H. Wang, "Generation of narrow-band polarization-entangled photon pairs at a rubidium D1 line," J. Phys. Soc. Jpn. **85**, 124403 (2016).